Original Article

Special Issue on *Disaster Risk Reduction in Mountain Areas*

Behavioural analysis and dynamic simulation of the debris flow that occurred in Ganluo County (Sichuan, China) on 30 August 2020

LI Nuo-dong[1] https://orcid.org/0000-0001-6446-0282; e-mail: linuodong@cqu.edu.cn

LIU Wei[2,3,4*] https://orcid.org/0000-0001-6336-4387; e-mail: spon@imde.ac.cn

ZHAO Jin-heng[5] https://orcid.org/0000-0002-4189-3146; e-mail: xiong_89510@163.com

*Corresponding author

1 Chengdu Power Supply Company of State Grid Sichuan Electric Power Company, Chengdu 610041, China

2 Key Laboratory of Mountain Hazards and Surface Process, Institute of Mountain Hazards and Environment, Chinese Academy of Sciences, Chengdu 610041, China

3 University of Chinese Academy of Sciences, Beijing 100049, China

4 State Key Laboratory of Hydraulics and Mountain River Engineering, Sichuan University, Chengdu 610065, China

5 Department of Water Hydropower and Construction Engineering, Skill Training Center of State Grid Sichuan Electric Power Company, Chengdu 610000, China

Abstract: On August 30, 2020, a high-intensity storm that dropped 45.4 mm of rain in 5 hours hit the Heixiluo basin and triggered a landslide-generated debris flow event, causing fatalities and damage. The original source of the debris flow was a large slope collapse on a steep hillside. The fallen debris mass was enlarged through sediment entrainment and slope collapse and ultimately buried a bridge at the gully entrance. Approximately 6.9×10^5 m^3 of material, including sediments and collapsed slope deposits in the gullies, was entrained, and the maximum erosion depth reached 17 m. A geomorphological analysis was initially performed based on a detailed field investigation to recognize the liquid and solid sources of the debris flow and the areas subjected to deposition and erosion. A map of the erosion-deposition distribution was obtained based on pre- and post-event DEMs. Using the rainfall estimated by the nearest rain gauge and the solid source estimated by the DEMs, runoff and debris flow propagation was simulated using a liquid-solid two-phase model that considers the effects of runoff and entrainment. The similarity between the estimated and simulated deposition-erosion volumes was satisfactory. The behaviour of debris flows captured in the simulation is broadly in line with the main features of the observed event.

Keywords: Debris flow; Formation analysis; Two-phase model; Dynamic simulation

1 Introduction

Landslide-generated debris flows are one of the most common types of mountain hazards (Iverson 1997) and pose a great threat to nearby facilities and residents. The formation of a landslide-generated debris flow can be simply divided into three stages: runoff generation, slope failure and debris flow routing (Bout et al. 2018; Liu et al. 2021). The first two stages do not have a fixed order, but their

sequence can largely determine the time scale of landslide-generated debris flows, which may occur within a few hours to many days. This is mainly because debris flows, unlike landslides, only occur with a sufficient source of water, such as heavy rainfall and ice/snow melt. A debris flow cannot be formed in the absence of a water supply when a landslide occurs, and such a feature would lengthen the time scale of landslide-generated debris flow. For instance, the number of debris flow events in the earthquake-affected area increases during the rainy season, although sufficient material sources always exist (Lin et al. 2004; Tang et al. 2009). Instead, landslides occurring during a rainstorm may quickly transform into a debris flow under the joint effects of the solid-fluid interactions (Fleming et al. 1989; Gabet and Mudd 2006), topography (Fernandes et al. 2004; Kang et al. 2017), and rainfall conditions (Gao et al. 2017; Peng et al. 2015). In such cases, the type of materials involved has a main role in determining the behaviour of slope process, and however, the difficulties of mitigating and preventing debris flow increase due to its short time scale.

Due to the complexity and unpredictable properties of this type of debris flow, interest has been high, and various mechanisms have been proposed to depict the motion behaviours and characteristics of these events (Iverson and George 2014; Liu et al. 2020; Luna et al. 2012; Pudasaini 2012). These mechanisms can successfully describe some phenomena that have been observed to occur in debris flow propagation, such as viscosity variation (Liu et al. 2020), pore water pressure evolution (Iverson and George 2014), and volume enlargement (Luna et al. 2012). Furthermore, focusing on the whole evolution process of debris flows, some comprehensive theories that couple the three stages of formation are established and validated by actual cases (Bout et al. 2018; Liu et al. 2021; Zhou et al. 2019), providing an effective way to study landslide-generated debris flows in more detail with the consideration of influencing factors such as runoff and sediment distribution. Over the past decades, the continuous development of mechanistic research and numerical technology has improved the availability of numerical modelling for the quantitative assessment of debris flows (Gregoretti et al. 2019; Liu et al. 2021; Stancanelli et al. 2017). Nevertheless, when a debris flow event occurs, to generate an in-depth understanding of the debris flow and the possible

governance approach, it is necessary to determine the cause and the corresponding mechanism by conducting field surveys and analysis. In that way, the result of inverse modelling will be more accurate.

In this paper, the geological conditions, causes and main characteristics of the landslide-generated debris flow that occurred at Heixiluo gully on August 30, 2020, in Ganluo County, Sichuan, China, are investigated based on a comprehensive investigation including field surveys, remote sensing data, unmanned aerial vehicle (UAV) image data and numerical simulation. According to the field survey, the volume of debris flow increased significantly during the propagation process, and entrainment and slope collapse were considered to be the primary causes. To better understand how entrainment, topography, and runoff affect the propagation of debris flows, a two-phase depth-averaged model taking entrainment into account is applied for simulation. The results of this event aim to provide both a deeper understanding of this type of debris flow and further geological hazard alleviation measures.

2 Data and Methods

2.1 Geological setting

Ganluo County is located in western Sichuan, spanning from the Sichuan Basin to the Qinghai-Tibet Plateau. Influenced by the Hengduan Mountains, this area has a typical canyon geomorphology, such as a narrow valley, rugged terrain and obvious vertical change in climate. The eastern margin of the Qinghai-Tibet Plateau is also a region with very steep topography, with intense internal and external dynamic effects, and extremely frequent weather changes, exhibiting the most extreme features in China and possibly even the world (Ni et al. 2021; Zhang and Wu 2012). In addition, this area borders the Xianshuihe Fault Zone that is prone to frequent and strong seismic activity. These complex geological conditions lead to the fragmentation of mountain structures and frequent geological disasters in this region. According to the 1:2000000 geological map made by the Sichuan Geological Survey (Fig. 1), the strata exposed in the Heixiluo basin include a) the pre-Sinian (Pt_1eb^{2-3}), which consists of marble, slate and metamorphic sandstone, and b) the Sinian
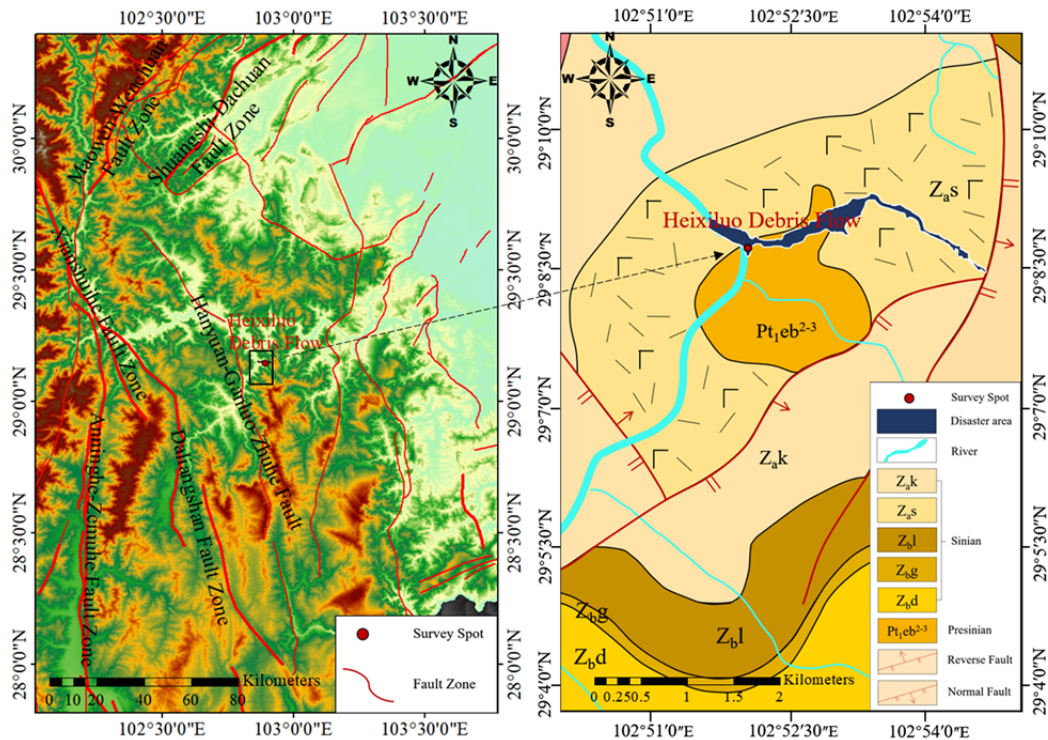
Fig. 1 Regional tectonic sketch map of a) the distribution of fault zones in southwest Sichuan and b) the study area.

Suxiong Formation (Z_as-K), which consists of Anshan basalt, Anshan porphyry and pyroclastic rock. In the Heixiluo basin, the sediment materials are quaternary fluvial sediments. The exposed bedrock is seriously affected by weathering, and most of the slopes are soil-rock mixed slopes with poor stability. Broken rock masses and loose surface sediments provide favourable material source conditions for the formation of debris flows.

2.2 Overview of the events

On August 30, 2020, a landslide-generated debris flow occurred at Heixiluo gully, Ganluo County, in Sichuan Province, Southwest China (29°08'35.93"N, 102°52'9.33"E), which buried a bridge of the ChengKun railway and temporarily blocked the Niri River (Fig. 2a). After the debris flow, a detailed investigation was carried out on the cause and propagation of this debris flow through field surveys and terrain data collection. High-resolution digital elevation models (DEMs) and digital orthophoto maps were obtained by using high-performance UAV photogrammetry collected on November 11, 2020, and ALOS PALSAR Hi-Res Terrain Corrected data collected on September 16, 2010. Based on a comparison of pre- and post-event

DEMs, this debris flow displaced 4.8×10^5 m³ of material derived from the landslide in the source area, and its final volume was 11.7×10^5 m³ under the effects of entrainment ($\approx 6.9 \times 10^5$ m³). This indicates that most of the debris flow materials were entrained sediment. The debris flow runout extended 4000 m horizontally and 977 m vertically and covered an area of en4.84×10^5 m². After the debris flow event, the ground of Heixiluo gully changed significantly, which manifested slope collapse and sediment entrainment (Fig. 2b).

Unfortunately, the rainfall intensity that contributed directly to the event in the Heixiluo basin is lack and the data collected at the rain gauge installed in the nearby village is used, as depicted in Fig. 3. This village is located in the northwestern Heixiluo basin and is approximately 1700 m from the centroids of the Heixiluo basin. Fig. 3 shows the records of hourly rainfall from 01:00 to 23:00 on 30 August 2020. The rainfall was mainly concentrated from 19:00 to 23:00 on 30 August, with a total of 45.4 mm of accumulated rainfall. The corresponding mean intensity was 9.08 mm/h, while the largest intensity was 15 mm/h. The debris flow was triggered at 20:00 on 30 August 2020. This rainfall event with a short duration and high intensity is a typical precipitation event causing landslide-generated debris flows that
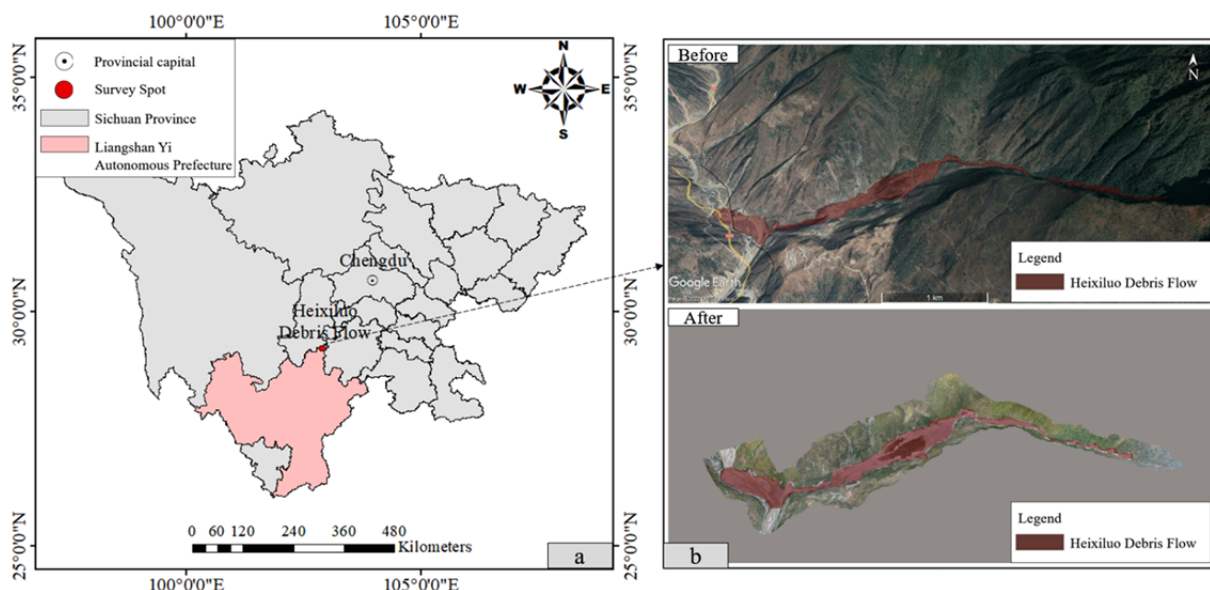
Fig. 2 a) Location map of the Heixiluo basin and b) its landscape before and after the debris flow event.

occur along western Sichuan.

2.3 Characteristics of the debris flow

To provide more direct and comprehensive knowledge of this debris flow event, a terrain model was reconstructed by ALOS PALSAR 12.5-m Hi-Res Terrain Corrected images collected by UAV. Combined with the terrain model and the site survey, the debris flow affected zone, the distribution of erosion depth and the collapsed slope can be described. Here, we divided the debris flow-affected area into five reaches due to their unique features.

I. Source Area. This reach has a narrow channel with a slope of 13° and covers an area of approximately 3.2×10^4 m², which favours runoff generation. The source material of debris flow came from a collapsed slope that was located at an altitude of 1700 m and had an averaged thickness of 15 m (maximum thickness reaches 40 m) and a volume of 4.8×10^5 m³.

II. Propagation Area A. The collapsed mass mixed with runoff formed a debris flow and propagated downstream along the steep channel. Quaternary sediments and heavily weathered pre-Sinian and Sinian bedrock on the channel surface were heavily eroded by the debris flow. The average erosion thickness in this reach is approximately 5 m (maximum erosion depth is up to 17 m). This propagation reach covers an area of approximately 8.2×10^4 m². An interesting phenomenon is that there

is a 45° corner between propagation area A and the next reach; however, the height of coverage of the debris flow at this corner is less than 10 m, and there is no mass overflow on the other side of the corner (Fig. 4a and Fig. 5a). It indicates that the debris flow mass passed this corner at a low speed.
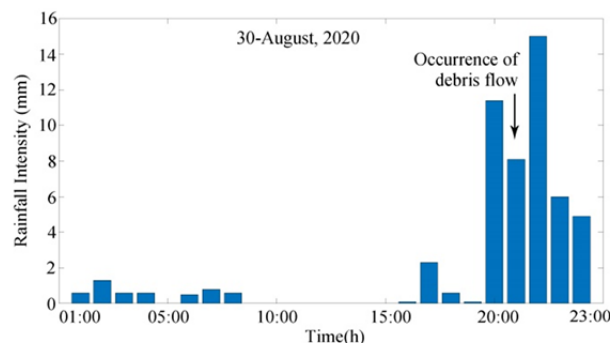

Fig. 3 Hourly rainfall data from 01:00 to 23:00 on 30 August 2020 obtained from the rain gauge installed in the village nearby Heixiluo basin.

III. Accumulated & Restarted Area. This reach covers an area of approximately 6.8×10^4 m² and has an open and flat deposition platform. Therefore, the debris flow had a low speed in this area and partially stopped on the right side and front end of the platform, and part of the debris mass overflowed into the hilly area downslope (Fig. 5b). The major components of the deposits are Quaternary sediment, granite and basalt, which is further evidence that the debris materials mainly come from collapsed bedrock and eroded surface sediment. Additionally, some characteristics of the debris materials can be

identified from the deposits, such as a high mud content and poor gravel roundness (maximum diameter is up to 12 m) (Fig. 5c). The debris deposits increased the elevation of the middle and right sides of this reach, which forced the subsequent flow to propagate into the left side of this reach. With more debris mass and rainwater accumulation, the debris mass overcame the restriction of the terrain and propagated into the next reach.

IV. Propagation Area B. Serious erosion occurred in the upper part of this reach, to an average depth of 7 m, which was caused by the debris flow restarting and reaching a high speed. Five slopes collapsed due to serious erosion and were incorporated into the debris flow. Here, although a part of this reach is relatively flat, only a small amount of debris materials accumulated, and most of the debris materials propagated downstream and increased the elevation of the bed channel approximately 10 m from the gully entrance. There was a sudden increase in slope at the middle of this reach (Fig. 4b), which also favoured debris flow propagation. This reach covers an area of approximately 1.12×10^5 m².

V. Accumulated Area. The debris flow finally piled up at the gully entrance, and the average thickness of the deposit is approximately 5 m (Fig. 5d). The debris deposits buried a bridge of the ChengKun railway, and the rest of the debris mass blocked the Niri River, which formed a temporary debris dam that was washed away by the river flow after several hours. Several houses were also destroyed by the debris flow. The area of this reach is close to that of propagation area B and is approximately 1.9×10^5 m².

2.4 Numerical modelling

In this section, the model used for simulating rainfall-induced runoff and debris flow propagation is presented. As a typical solid-fluid flow, debris flows capture the fluid phase from rainwater and the solid phase from surface sediments and slope failure. According to this feature of debris flows, a two-phase model proposed by Liu et al. (2021) is adopted. This two-phase model provides two advantages: first, it describes the solid and fluid phases separately to reflect the interaction of the solid and fluid, e.g., the drag force, more directly (Pitman and Le 2005; Pudasaini 2012); second, it has the capacity to join two stages of runoff and debris flow propagation. For example, before slope failure, a two-phase model can be used like a single-phase model to simulate runoff by neglecting the solid phase. However, either the runoff or debris flow propagation is highly complex and challenging to simulate using a full three-dimensional model that involves all behaviours. To focus on the main behaviours of these two stages, a depth-averaged form of a two-phase model is used for simulation. This model reduces the complicated three-dimensional Navier–Stokes equations into a simple two-dimensional continuum problem by neglecting the changes in the vertical direction due to the large aspect ratio of the runoff and debris flow; in
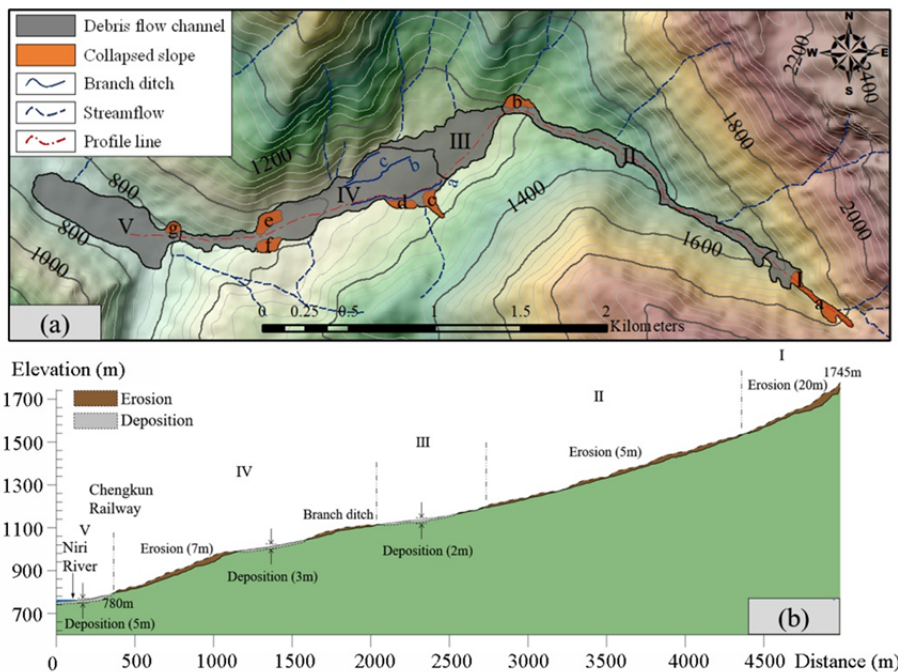

Fig. 4 Sketch map of the debris flow studied and its local features. a) The impact area was divided into five reaches: Ⅰ. source area; Ⅱ. propagation area A; Ⅲ. accumulated & restarted area 2; Ⅳ. propagation area B; Ⅴ. accumulated area. b) A topographical profile where the different parts of the debris flow path affected by erosion and deposition are indicated.

Fig. 5 a) Field observation of the landscape in the corner (propagation area A), which indicates that the speed of the passing debris flow was relatively slow; b) the debris flow overrunning phenomenon occurred in the accumulated & restarted area; c) the largest particle size (approximately 12 m in diameter) found in the area accumulated & restarted area; d) aerial view of the debris deposits at the gully entrance and the nearby buried house.

other words, if its lateral extension was large compared to the thickness of the layer (Savage and Hutter 1989). This approach has been validated by a series of experimental benchmarks and case studies (Liu et al. 2021; Meng et al. 2016). A field investigation has indicated that entrainment was the main factor that influences the propagation behaviour of the Heixiluo debris flow and is therefore considered in the model. Here, we assume that the eroded materials mixed well with the debris flow and that its properties were the same as those of the debris flow, which is helpful for highlighting the effect of entrainment on debris flow propagation while neglecting some unique phenomena, e.g., dilatancy. A local Cartesian coordinate system is used (Pitman and Le 2005), in which the x-axis is parallel with the bed surface and the positive x-axis is directed downdip, the y-axis lies in the cross direction, and the z-axis is orthogonal to both the x- and y-axes. Detailed topographic effects can be included via the gradients of the basal topography in the x- and y-directions (Fischer et al. 2012). The governing equations, based on the conservation of mass and momentum, can be expressed as (Liu et al. 2021)

$$\frac{\partial(\alpha_s h)}{\partial t} + \frac{\partial(\alpha_s h u_s)}{\partial x} + \frac{\partial(\alpha_s h v_s)}{\partial y} = R_s + E_s,$$

$$\frac{\partial(\alpha_s h u_s)}{\partial t} + \frac{\partial\left(\alpha_s h\left(u_s^2 + 0.5\beta_{xs}h\right)\right)}{\partial x} + \frac{\partial(\alpha_s h u_s v_s)}{\partial y}$$

$$= u_s^b E_s + h\left[\begin{array}{c} \alpha_s\left(g_x - \dfrac{u_s}{|\mathbf{u}_s|}p_{bs}\tan\varphi_{bed} - \varepsilon p_{bs}\dfrac{\partial z_b}{\partial x}\right) \\ -\varepsilon\alpha_s\gamma p_{bf}\left(\dfrac{\partial h}{\partial x} + \dfrac{\partial z_b}{\partial x}\right) \end{array}\right] + \frac{f_{dx}}{\rho_s},$$

$$\frac{\partial(\alpha_s h v_s)}{\partial t} + \frac{\partial(\alpha_s h u_s v_s)}{\partial x} + \frac{\partial\left(\alpha_s h\left(v_s^2 + 0.5\beta_{ys}h\right)\right)}{\partial y}$$

$$= v_s^b E_s + h\left[\begin{array}{c} \alpha_s\left(g_y - \dfrac{v_s}{|\mathbf{u}_s|}p_{bs}\tan\varphi_{bed} - \varepsilon p_{bs}\dfrac{\partial z_b}{\partial y}\right) \\ -\varepsilon\alpha_s\gamma p_{bf}\left(\dfrac{\partial h}{\partial y} + \dfrac{\partial z_b}{\partial y}\right) \end{array}\right] + \frac{f_{dy}}{\rho_s},$$

$$(1)$$

$$\frac{\partial\left(\alpha_f h\right)}{\partial t}+\frac{\partial\left(\alpha_f h u_f\right)}{\partial x}+\frac{\partial\left(\alpha_f h v_f\right)}{\partial y}=R_f+E_f,$$

$$\frac{\partial\left(\alpha_f h u_f\right)}{\partial t}+\frac{\partial\left(\alpha_f h u_f^2\right)}{\partial x}+\frac{\partial\left(\alpha_f h u_f v_f\right)}{\partial y}$$

$$=u_f^b E_f+h\alpha_f g_x$$

$$-h\alpha_f\varepsilon\left[\frac{1}{h}\frac{\partial}{\partial x}\left(\frac{h^2}{2}p_{bf}\right)+p_{bf}\frac{\partial z_b}{\partial x}\right]-\alpha_f g_z\frac{n_b^2}{h^{1/3}}u_f\left|\mathbf{u}_f\right|-\frac{f_{dx}}{\rho_f}$$

$$+\varepsilon h\left[\frac{1}{N_R}\left(2\frac{\partial^2 u_f}{\partial x^2}+\frac{\partial^2 v_f}{\partial y\partial x}+\frac{\partial^2 u_f}{\partial y^2}-\frac{\chi u_f}{\varepsilon^2 h^2}\right)+\frac{\xi\alpha_s\left(u_f-u_s\right)}{\varepsilon^2 N_{RA}h^2}\right],$$

$$\frac{\partial\left(\alpha_f h v_f\right)}{\partial t}+\frac{\partial\left(\alpha_f h u_f v_f\right)}{\partial x}+\frac{\partial\left(\alpha_f h v_f^2+0.5\varepsilon g_z\alpha_f h^2\right)}{\partial y}$$

$$=v_f^b E_f+h\alpha_f g_y-h\alpha_f\varepsilon\left[\frac{1}{h}\frac{\partial}{\partial y}\left(\frac{h^2}{2}p_{bf}\right)+p_{bf}\frac{\partial z_b}{\partial y}\right]$$

$$-\alpha_f g_z\frac{n_b^2}{h^{1/3}}v_f\left|\mathbf{u}_f\right|-\frac{f_{dy}}{\rho_f}$$

$$+\varepsilon h\left[\frac{1}{N_R}\left(2\frac{\partial^2 v_f}{\partial y^2}+\frac{\partial^2 u_f}{\partial x\partial y}+\frac{\partial^2 v_f}{\partial x^2}-\frac{\chi v_f}{\varepsilon^2 h^2}\right)-\frac{\xi\alpha_s\left(v_f-v_s\right)}{\varepsilon^2 N_{RA}h^2}\right],$$

$$\tag{2}$$

$$\frac{\partial z_b}{\partial t}=-E=-\left(E_s+E_f\right). \tag{3}$$

where h is the flow depth; z_b is the bed surface; α_s denotes the volume fraction for the solid phase; and α_f denotes the volumetric fraction for the fluid phase, $\alpha_f = 1-\alpha_s$. Note that before slope failure, $\alpha_f = 1$ is applied to all the computation areas for simulating runoff. $\mathbf{u}_s = (u_s, v_s)$ and $\mathbf{u}_f = (u_f, v_f)$ are the velocities for the solid and fluid phases in the x and y directions, respectively; the aspect ratio ε is expressed as $\varepsilon = H/L$, where H is the typical depth and L is the typical topography-parallel length; $\gamma = \rho_f/\rho_s$ is the density ratio, where ρ_f and ρ_s are the densities of the fluid and solid phases, respectively; (g_x, g_y, g_z) are the gravitational acceleration components; $\mathbf{u}_s^b = (u_s^b, v_s^b)$ and $\mathbf{u}_f^b = (u_f^b, v_f^b)$ are the erosion velocities for the solid and fluid phases at the bottom boundary, respectively, which are associated with the erosion drift coefficients and the mean flow velocities (Pudasaini and Fischer 2020). n_b is the Manning friction coefficient; $E_s = (1-\theta_s)E$ and $E_f = \theta_s E$ are the solid and fluid entrainment rates, respectively. The premise of using this expression is that the sediments are saturated when they are eroded. θ_s is the sediment porosity; φ_{bed} is the Coulomb friction angle of the basal surface; and k_x and k_y are the earth pressure coefficients. Other parameters involved in the model equations are $\beta_{xs} = \varepsilon k_x p_{bs}$, $\beta_{ys} = \varepsilon k_y p_{bs}$, $\beta_{xf} = \beta_{yf} = \varepsilon p_{bf}$, $p_{bs} = (1-\gamma)p_{bf}$, $p_{bf} = $

$-g_z$, $N_R = \rho_f H(gL)^{0.5}/(\alpha_f\mu_f)$, $N_{RA} = \rho_f H(gL)^{0.5}/(A\mu_f)$. A is the mobility of the fluid at the interface and can be treated as a phenomenological parameter; χ refers to the fluid velocity of vertical shearing; ξ is the shape factor that takes into account different distributions of α_s (Pudasaini 2012); μ_f is the fluid viscosity; R_s is the solid mass from the slope failure; R_f is the fluid mass from the rainfall event. $\mathbf{f}_d$ is the drag force between two phases, and here, a formula proposed by Pitman and Le (2005) based on the experimental data is adopted to express this force:

$$\mathbf{f}_d = \frac{h(\rho_s-\rho_f)\alpha_s\alpha_f}{V_T\alpha_f^{M_e}}\left(\mathbf{u}_f-\mathbf{u}_s\right) \tag{4}$$

where V_T is the terminal velocity of a particle falling in a fluid and the value of M_e varies from approximately 4.65 to 2.4 as the Reynolds number increases from zero to infinity (Pitman and Le 2005). Eq. (4) produces a singularity as α_f trends to 0, so the unboundedness of the drag is cut off by considering a threshold in this work. The entrainment rate E can be expressed as follows (Liu and He 2017):

$$E = -\frac{\partial z_b}{\partial t} = \frac{\tau_b-\tau_r}{\rho_m\sqrt{u_m^2+v_m^2}} \tag{5}$$

where $u_m = \alpha_s u_s + \alpha_f u_f$ and $v_m = \alpha_s v_s + \alpha_f v_f$ are the phase-averaged variables; the total basal shear traction τ_b is considered $\tau_b = \alpha_s\tau_{bs} + \alpha_f\tau_{bf}$, where $\tau_{bs} = (\rho_s-\rho_f)g_z h\tan\varphi_{bed}$ is the basal shear stress for the solid phase and $\tau_{bf} = \rho_f g_z n_b^2\ \mathbf{u}_f|\mathbf{u}_f|/h^{1/3}$ is the basal shear stress for the fluid phase. This form of τ_b combines the Coulomb friction model and Manning model to better describe the basal shear stress of flow with a variation in the solid volume fraction. $\tau_r = c_p+\rho_m(1-\eta)g_z h\tan\varphi_{int}$ is the sediment shear resistance from the erodible sediment, where c_p is the soil effective cohesion and φ_{int} is the internal friction angle of the sediment material; η is the pore pressure ratio that indicates the degree of liquefaction of the sediments from a dry state ($\eta = 0$) to a fully liquefied state ($\eta = 1$); and $\rho_m = \alpha_s\rho_s + \alpha_f\rho_f$ is the density of the debris flow mixture. Equation (5) also produces a singularity as the mass flow stops, and this singularity is avoided by assuming that entrainment will not happen if the flow velocity is smaller than a setting value. More details and explanations about the presented model can be found in Liu et al. (2021).

A numerical scheme consisting of the finite volume method (FVM) and Riemann approximation solver is applied to manage the governing equations

(Loukili and Soulaïmani 2007). To preserve a steady state between the flux and source terms during calculation, a well-balanced scheme proposed by Audusse et al. (2004) is implemented. In addition, the local bed slope and variables such as depth and velocity are modified at the wet or dry fronts to prevent non-physical flux generation (Liang and Borthwick 2009). The time step is computed according to the Courant-Friedrichs-Lewy stability conditions (Gnedin et al. 2018). The variables of the solid and fluid phases are computed for each cell with Eqs. (1) and (2) and are used in Eq. (3) to provide the rate of change in bed elevation.

2.5 Topographic data processing

The ALOS PALSAR 12.5-m Hi-Res Terrain Corrected data can be used in the numerical simulation of a gully debris flow, which can basically reflect the overall movement of a debris flow; additionally, by processing the existing DEMs, we can effectively analyse the overall characteristics of the debris flow and estimate the volume of the priming source (Tang et al. 2019). However, because the Heixiluo debris flow has unique properties at branch ditches and collapsed piles, the 12.5 m accuracy of the original terrain did not fully reflect this, so the following was performed to determine the original terrain: (a) ArcGIS software was used to partition the debris flow and grid the XYZ grid data of the pre-event DEMs and the post-event DEMs into a 5 m grid in Surfer software (version Ⅰ). The source area was replaced with post-event mesh terrain data in the original terrain grid by Grid Mosaic in Surfer software. The difference between the pre-event and the post-event grid data in this area is used as the material volume for debris flow initiation. (b) According to the Google images captured and site investigation performed before the disaster, there were three obvious branches in reach Ⅳ. Propagation area B and the further erosion and confluence of the branches played an important role in the expansion of the
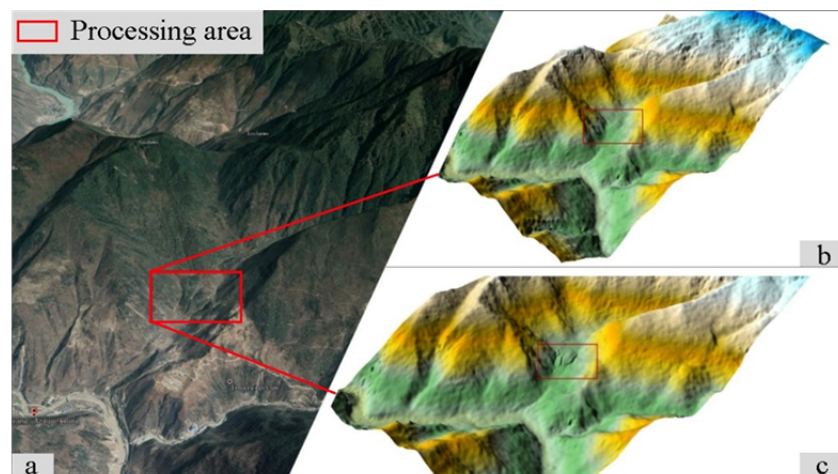

Fig. 6 Processing of the branch ditches in reach Ⅳ. Propagation area B: a) pre-disaster image from Google Earth; b) pre-event ALOS PALSAR DEM; c) pre-disaster DEM after processing.

debris flow. Unfortunately, the initial DEM with a 12.5 m accuracy could not display these features well. Combined with field investigation and reconstruction of the 3D model, we reset the elevation value of the debris flow channel erosion surface for the filling treatment (Fig. 6).

3   Results

This section aims to reproduce the entire formation process of debris flows with models through two components: hydrological modelling and debris flow propagation modelling. Hydrological modelling provides runoff hydrographs that directly contribute to the fluid phase of debris flows. A small amount of sediments may be eroded by runoff before forming debris flows; however, this phenomenon is neglected since slope failure is the major source of the initial debris materials. Similar to the runoff, the collapsed mass directly contributed to the solid phase when debris flow passing by. Properties of both the runoff and collapsed mass are used as inputs for debris flow propagation modelling. A 5-m grid terrain data that is modified from the ALOS PALSAR 12.5-m Hi-Res Terrain Corrected pre-event DEM and 0.5-m UAV post-event DEM is used in simulation. With that, a uniform size of 5m and a total number of 1.6 million for the computational grid are used in simulation.

3.1 Hydrological simulation

The rainfall-induced runoff modelling for the

Heixiluo basin depicted in Fig. 1 is carried out by the presented model with $\alpha_f = 1$. The model calculates the flow discharge at each computational cell of the basin and routes it through the optimal path to the main gully. The parameters considered in the runoff calculation are rainfall intensity R_s and Manning friction coefficient n_b. In general, the mass from the rainfall in the runoff is influenced by the soil properties and vegetation conditions (Bagarello et al. 2014; Patle et al. 2019; Puigdefábregas 2005; Rengers et al. 2016). However, the mechanisms of these influences are complex and remain unclear, and for simplicity, we assume that the mass from the rainfall event equals the rainfall intensity. Two typical values of n_b, 0.15 and 0.03, corresponding to vegetated ground and bare ground, are assigned to a computational cell (Cui et al. 2013; Han et al. 2017). Runoff hydrographs for the three record points (marked by stars) located in the Heixiluo basin are presented in Fig. 7a, with observed uniform rainfall from 01:00 to 23:00 on 30 August applied to the whole area. During this period, tributaries were formed and further collected into runoff along the steep terrain. The runoff amount was enhanced in the key period between 16:00 and 23:00 on 30 August.

This may be one of the important factors affecting the stability of slopes that contributes to the solid phase of debris flows. Furthermore, it is worth noting that a pool of water was formed in the middle of propagation area A (Fig. 7b), which means that there exists a concave terrain that favours debris flow accumulation. On the other hand, a dam break flow can be formed and causes serious erosion of the downstream channel if a breach is generated by flow overtopping. As shown in Fig. 5b, a breach occurred, and the adjoining terrain was seriously eroded. Thus, we can speculate that a dam-break debris flow has occurred and that this process enhances the mobility and impact of a debris flow downstream.

3.2 Debris flow propagation simulation

The sites on the Heixiluo basin where the slope collapsed after the impact of the runoff with the debris deposits could not be surveyed because of their inaccessibility. Therefore, we determined that the time when slope collapse occurred in the source area was 20:00 on 30 August. For the other five slopes, we assumed that they collapsed when the debris flow passed through their toe. Parameters of debris flow
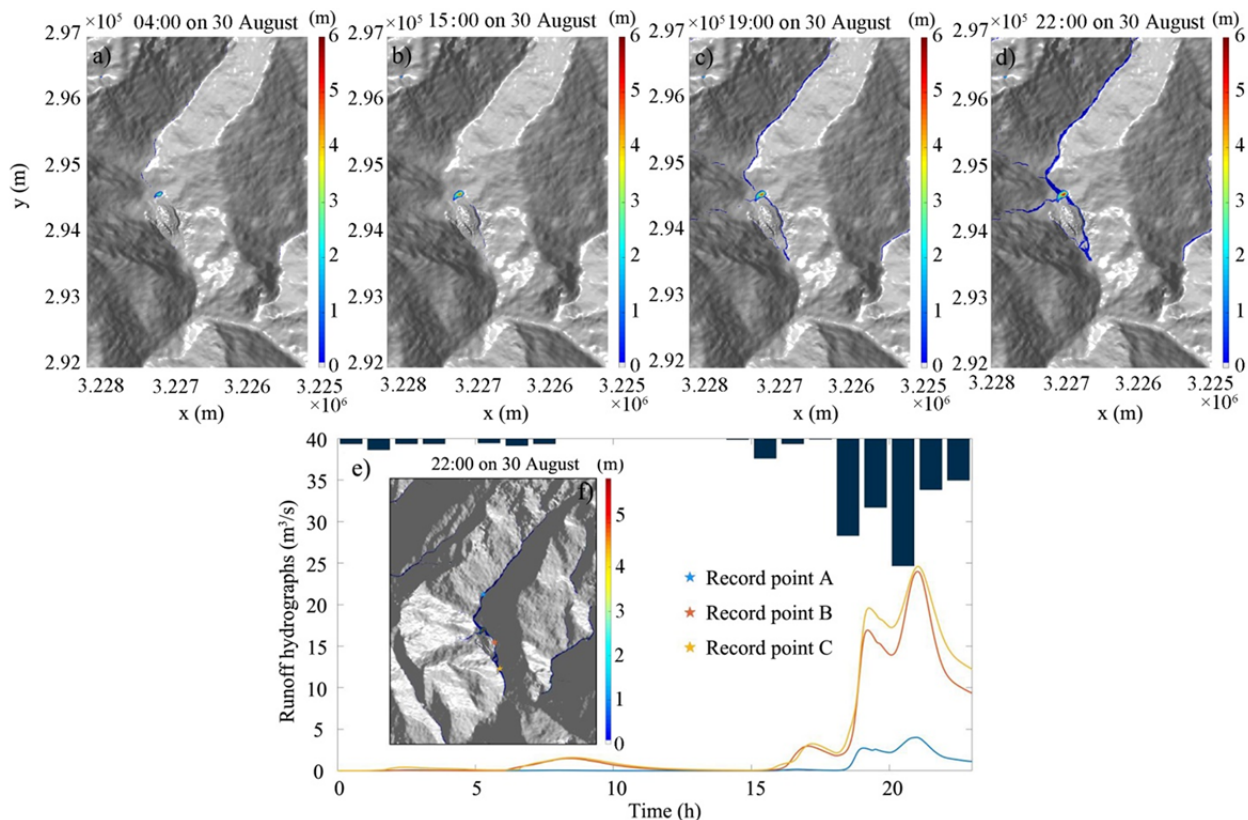

Fig. 7 Process of runoff generation (a-d) and modelled runoff hydrographs for the three record points located in the Heixiluo basin corresponding to the measures of rainfall intensity (e-f). The colour bar represents the flow depth (m).

propagation simulation depend on the terrain and slope materials and sediments because flow properties, deposition and entrainment processes vary with them. Fig. 6b shows the land use of the terrain obtained from the pre- and post-event DEMs. The values of the parameters used for the propagation simulation are shown in Table 1. This set of parameters was determined based on field investigation and the comparison between observations and simulations of deposition and erosion depths and impact areas.

The simulated debris flow propagation results at different times are shown in Fig. 8. For a better comparison between the estimates of the deposited and eroded sediment volumes, the flow pattern was divided into five reaches corresponding to the reaches mentioned above. In particular, both the estimated deposition and erosion depths are shown in four reaches (Fig. 4), II-V, allowing a more detailed analysis together with a table of the values of the estimated and simulated sediment volumes (Fig. 9) that were eroded and deposited for each reach. The comparison of the simulation results with the observations shows that the main features of the flow pattern are captured by the presented method except at the gully entrance where the terrain is flat and adjoins the Niri River. The simulated volumes of the eroded and deposited materials are 4.7×10^5 m³ and 12.4×10^5 m³, respectively, which are overestimations by approximately 7.4% and 6.2%. This overall satisfactory agreement between the simulations and observations was a validation of the presented model used here for simulating solid-liquid flows. The examination of the results reach by reach allows a

better understanding of the model capability to simulate the phenomenon that occurred. In reach II, the simulated eroded material volume somewhat coincides with the estimated eroded material volume, and both correspond to a deep eroded depth. This could be because the narrow path of reach II forces the simulated debris flow to concentrate and therefore results in heavy erosion. Regarding deposition, the small deposits in this zone are not satisfactorily reproduced because the local bed slope of the terrain is not captured in the pre-event DEM. Debris flow materials that were not deposited there during the simulation were deposited just downstream of the confluence (beginning of reach III). In fact, the deposition depth in this zone is on average much smaller than the estimated eroded depth according to the field investigation. Routing along reach III was satisfactorily simulated with an average deposition depth of 2.5 m, which reflects a good agreement between the observations and simulations. After the deposits uplifted the elevation of the middle and right sides of this reach, the debris mass propagated into reach IV along the right side first and then along the middle and right sides of reach III. In reach IV, the agreement between the simulated and estimated deposition and erosion volumes is not satisfactory (the percentage of simulated erosion volume is 8% larger than that observed). Nevertheless, the areas subjected to the main deposition and erosion phenomena nearly coincide. For reach V, the agreement is satisfactory for both the flow pattern and the volumes, although the simulated volume of the deposits is underestimated compared with that estimated (approximately 5%). Fig. 9 shows the

Table 1 The parameters used in the model, their values, and sources.

| Input data	Parameter	Value	Source
Rainwater density	ρ_f	1000 kg/m³	Liu et al. (2021)
Pure fluid viscosity	μ_f	0.065 Pa·s	Rutgers (1962)
Basal coulomb friction angle	φ_{bed}	22°	Measured
Solid density	ρ_s	2700 kg/m³	Measured
Soil effective cohesion	c_p	2100 Pa	Measured
Sediment porosity	θ_s	0.4	Measured
Soil internal friction angle	φ_{int}	35°	Measured
Pore pressure ratio	η	0.6	Ouyang et al. (2015)
Manning friction coefficient	n_b (vegetated ground)	0.15 s/m$^{1/3}$	De Doncker et al. (2009)
	n_b (bare ground)	0.03 s/m$^{1/3}$	De Doncker et al. (2009)
Gravitational acceleration	g	9.8 m/s²	Pitman and Le (2005)
Solid-fluid drag force coefficient	M_e	3	Pitman and Le (2005)
Particle terminal velocity	V_T	1	Pitman and Le (2005)
Velocity shape factor	ξ	3	Pudasaini (2012)
Solid distribution shape factor	χ	5	Pudasaini (2012)
Aspect ratio	ε	1	Pudasaini (2012)
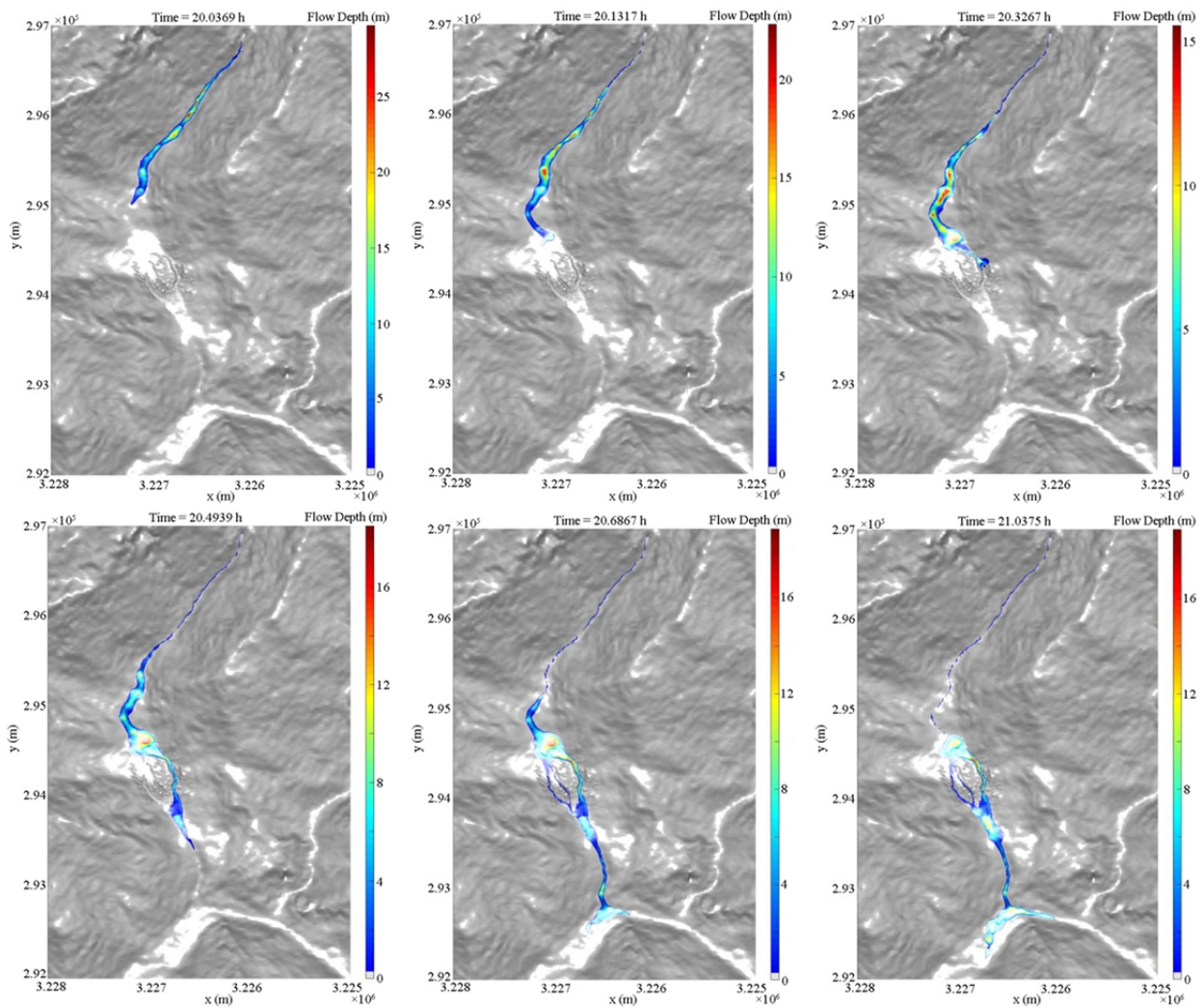
Fig. 8 Propagation process of the studied debris flow in the Heixiluo basin at different times. The colour bar represents the flow depth (m).

simulated erosion pattern and the solid-liquid discharge after the debris flow occurred. After the collapse of the slope in reach I, the debris flow discharge peak at record point A has the maximum value. However, the debris flow at in record point B is reduced to less than 80% due to the large deposition phenomena, which are mostly controlled by the local terrain features. A record point C, the small discharge in the first half hour is liquid because of the runoff confluence and reaches the peak caused by the collapse of the slope on both sides of the gully.

4 Discussion

4.1 Applied method

In this paper we applied a two-phase model that

incorporates the effect of entrainment to simulate the formation process of Heixiluo debris flow. Comparing with previous studies (Ouyang et al. 2015; Pitman and Le 2005; Pudasaini 2012), the applied model could describe the characteristics of runoff and debris flow simultaneously by defining some judgement conditions. For a calculation grid, the applied rheological model for fluid phase varies with the value of solid volume fraction α_s. The Manning friction law is applied to runoff ($\alpha_s=0$) and the fluid phase of debris flow ($\alpha_s<0.2$) (Beverage and Culbertson 1964). Otherwise, the viscous friction law is used to relfect the behaviour of the fluid phase of debris flow (Iverson and Denlinger 2001; Pudasai 2012). This approach is also in favour of entrainment calculation since a more accurate basal shear force from the fluid phase of debris flow can be obtained and further applied in Eq. (5).
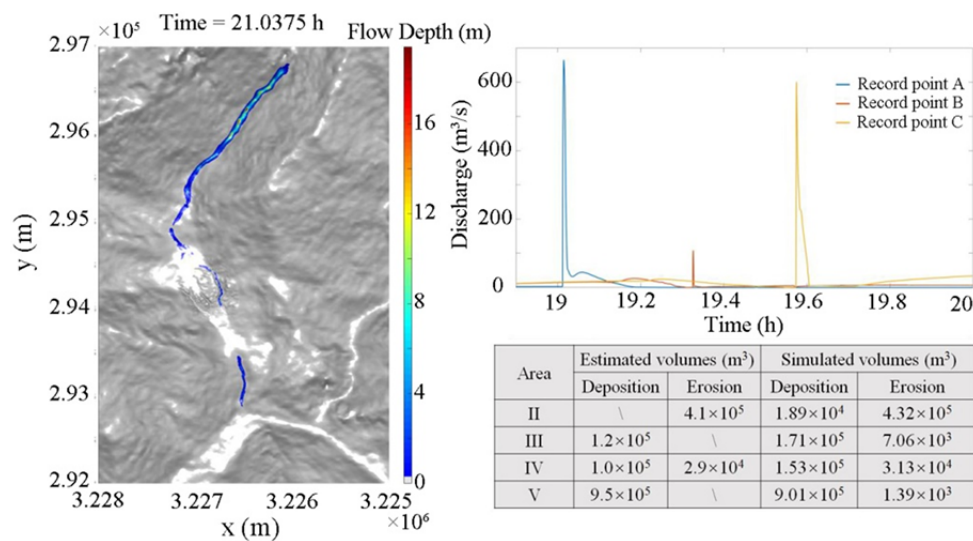
Fig. 9 Simulated erosion pattern (left), hydrographs of solid-liquid discharge (upper right), erosion and deposition volumes compared with the estimated volumes (lower right). Locations of record points A, B and C have been shown in Fig. 7.

4.2 Reliability and uncertainty of the results

The back-analysis of the debris flow shown in the previous section appears to be satisfactory in general. Apart from some parts of reaches II and IV, the deposition and erosion pattern is well reproduced both in terms of areas and volumes. One reason for this finding is the low accuracy of terrain data. The estimated data are obtained based on pre- and post-event DEMs. Unfortunately, the pre- and post-event terrain was subjected to excavation during the restoration works in the month between the data collection time and the event. Some paths and flat areas (especially those of the gully surfaces in reaches IV and V) built by excavators could have conditioned the flow propagation and led to data error. The simulations in reaches II and IV are conditioned by pre-event topographical data that have a 5-m resolution and thus are inaccurate because they only partially reflect local terrain features. As a consequence, the deposition in this area was not captured. Moreover, the presence of rivers (in reach V) may have an important impact on debris flow accumulation, due to processes such as river channel terrain restriction and fluvial scouring. Therefore, the availability of pre- and post-event data is key for reliable simulation results and for a deeper understanding of debris flow behaviour (Gregoretti et al. 2018). The contribution of the collapsed mass incorporated into the debris flow is also key. Here, only a simple assumption was applied to these

collapsed slopes; however, the collapse time and collapse sequence of these slopes also could have had an important impact on debris flow propagation, especially at reach IV. The satisfactory and reliable reproduction of the event provides a confirmation that the presented approach can simulate a landslide-generated debris flow from runoff generation to debris flow propagation while considering sediment entrainment.

4.3 Limitation and future work

The present back analysis work of debris flow behaviour is important since it supplements the details of debris flow propagation that cannot be obtained from field investigation and provides a framework for predicting or preventing other debris flow events with similar conditions. Notably, the values of the parameters used for running the models were generally determined by comparing the field observations, estimated data and simulation results. These parameters keep a constant in simulation, and however, it would be preferable to determine the values of these parameters by flow state and dynamics rather than a set of fixed values for obtaining more accurately results of debris flow formation. In addition, the formation process of debris flow is complex and contains several stages that are closely related to each other (Bout et al. 2018; Liu et al. 2020). Some issues, e.g., the influence of vegetation

on runoff generation, sediment conservation and slope stability, still need to be further incorporated into the presented modelling approached based on mechanism analysis and in situ monitoring data collection. Further research on these aspects of the formation of debris flow and the improvement of multiphase model is required.

5   Conclusion

On 30 August 2020, a high-intensity storm hit the Heixiluo basin and triggered a channel debris flow that buried a bridge of the ChengKun railway and temporarily blocked the Niri River. This debris flow started after a slope collapse occurred during the storm and was of large magnitude, with approximately 6.90×10^5 m³ entrained materials. Direct field investigation and formation analysis of this debris flow allowed the recognition of the solid and liquid contributions to the debris flow and its main features and the mapping of the deposition and erosion volumes. Finally, the dynamic process of debris flow was modelled from rainfall-runoff transformation to debris flow propagation with satisfactory results. Most of the deposition and entrainment processes were captured; however, in some areas, the topography data were inaccurate due to the low accuracy of pre-event DEMs and anthropogenic disturbance. Based on these analyses and modelling results, the causes, dynamic process and contributing factors of the studied debris flow were presented. A detailed field investigation provided a guide for the implementation of models to simulate the evolution processes of debris flows and determining the initial conditions of the models. The two main contributing factors for this debris flow event were sediment entrainment and slope collapse. The former enlarged the scale of debris flow, and the latter provided the initial mass source and input energy into the system during flow propagation. Local terrain features partially determine the presence of debris deposits. Furthermore, the satisfactory results obtained in the reproduction of the debris event suggest that a two-phase model can be used for simulating all the evolution processes of a debris flow with the consideration of the rainfall-generated runoff, slope collapse and sediment entrainment. The capability of the models used to capture the main features of this debris flow event and the entrainment and deposition processes that occurred during debris flow propagation was validated by comparing the simulation results with the estimated data.

References

Bagarello V, Castellini M, Di Prima S, et al. (2014) Soil hydraulic properties determined by infiltration experiments and different heights of water pouring. Geoderma 213: 492-501. https://doi.org/10.1016/j.geoderma.2013.08.032

Beverage JP, Culbertson JK (1964) Hyperconcentrations of suspended sediment. J Hydraul Div 90(6): 117-128. https://doi.org/10.1061/JYCEAJ.0001128

Bout B, Lombardo L, van Westen CJ, et al. (2018) Integration of two-phase solid fluid equations in a catchment model for flashfloods, debris flows and shallow slope failures. Environ Modell Softw 105: 1-16. https://doi.org/10.1016/j.envsoft.2018.03.017

Cui P, Zhou GG, Zhu XH, et al. (2013) Scale amplification of natural debris flows caused by cascading landslide dam failures. Geomorphology 182: 173-189. https://doi.org/10.1016/j.geomorph.2012.11.009

De Doncker L, Troch P, Verhoeven R, et al. (2009) Determination of the Manning roughness coefficient influenced by vegetation in the river Aa and Biebrza river. Environ Fluid Mech 9(5): 549-567. https://doi.org/10.1007/s10652-009-9149-0

Fernandes NF, Guimarães RF, Gomes RA, et al. (2004) Topographic controls of landslides in Rio de Janeiro: field evidence and modeling. Catena 55(2): 163-181. https://doi.org/10.1016/S0341-8162(03)00115-2

Fleming RW, Ellen SD, Algus MA (1989) Transformation of dilative and contractive landslide debris into debris flows—an example from Marin County, California. Eng Geol 27(1-4): 201-223. https://doi.org/10.1016/0013-7952(89)90034-3

Fischer JT, Kowalski J, Pudasaini SP (2012) Topographic curvature effects in applied avalanche modeling. Cold Reg Sci Tech 74: 21-30. https://doi.org/10.1016/j.coldregions.2012.01.005

Gabet EJ, Mudd SM (2006) The mobilization of debris flows from shallow landslides. Geomorphology 74(1-4): 207-218. https://doi.org/10.1016/j.geomorph.2005.08.013

Gao Y, Yin Y, Li B, et al. (2017). Characteristics and numerical runout modeling of the heavy rainfall-induced catastrophic landslide–debris flow at Sanxicun, Dujiangyan, China, following the Wenchuan Ms 8.0 earthquake. Landslides 14(4): 1361-1374. https://doi.org/10.1007/s10346-016-0793-4

Gnedin NY, Semenov VA, Kravtsov AV (2018) Enforcing the Courant–Friedrichs–Lewy condition in explicitly conservative local time stepping schemes. J Comput Phys 359: 93-105. https://doi.org/10.1016/j.jcp.2018.01.008

Gregoretti C, Degetto M, Bernard M, et al. (2018) The debris flow occurred at Ru Secco Creek, Venetian Dolomites, on 4 August 2015: analysis of the phenomenon, its characteristics and reproduction by models. Front Earth Sci 6: 80. https://doi.org/10.3389/feart.2018.00080

Gregoretti C, Stancanelli LM, Bernard M, et al. (2019) Relevance of erosion processes when modelling in-channel gravel debris flows for efficient hazard assessment. J Hydrol 568: 575-591. https://doi.org/10.1016/j.jhydrol.2018.10.001

Han X, Chen J, Xu P, et al. (2017) A well-balanced numerical scheme for debris flow run-out prediction in Xiaojia Gully considering different hydrological designs. Landslides 14(6): 2105-2114. https://doi.org/10.1007/s10346-017-0850-7

Iverson RM, Reid ME, LaHusen RG (1997) Debris-flow mobilization from landslides. Annu Rev Earth Planet Sci 25(1): 85-138. https://doi.org/10.1146/annurev.earth.25.1.85

Iverson RM, Denlinger RP (2001) Flow of variably fluidized granular masses across three-dimensional terrain: 1. Coulomb mixture theory. J Geophys Res: Solid Earth 106(B1): 537-552. https://doi.org/10.1029/2000JB900329

Iverson RM, George DL (2014) A depth-averaged debris-flow model that includes the effects of evolving dilatancy. I. Physical basis. Proc R Soc A-Math Phys Eng Sci 470(2170): 20130819. https://doi.org/10.1098/rspa.2013.0819

Kang S, Lee SR, Vasu NN, et al. (2017) Development of an initiation criterion for debris flows based on local topographic properties and applicability assessment at a regional scale. Eng Geol 230: 64-76. https://doi.org/10.1016/j.enggeo.2017.09.017

Lin CW, Shieh CL, Yuan BD, et al. (2004). Impact of Chi-Chi earthquake on the occurrence of landslides and debris flows: example from the Chenyulan River watershed, Nantou, Taiwan. Eng Geol 71(1-2): 49-61. https://doi.org/10.1016/S0013-7952(03)00125-X

Liu W, He SM (2017) Simulation of two-phase debris flow scouring bridge pier. J Mt Sci 14(11): 2168-2181. https://doi.org/10.1007/s11629-017-4458-0

Liu W, He S, Chen Z, et al. (2020) Effect of viscosity changes on the motion of debris flow by considering entrainment. J Hydraul Res 59(1): 120-135. https://doi.org/10.1080/00221686.2020.1744746

Liu W, Yang Z, He S (2021) Modeling the landslide-generated debris flow from formation to propagation and run-out by considering the effect of vegetation. Landslides 18(1): 43-58. https://doi.org/10.1007/s10346-020-01478-4

Luna BQ, Remaître A, Van Asch TW, et al. (2012) Analysis of debris flow behavior with a one dimensional run-out model incorporating entrainment. Eng Geol 128: 63-75. https://doi.org/10.1016/j.enggeo.2011.04.007

McDougall S, Hungr O (2005) Dynamic modelling of entrainment in rapid landslides. Can Geotech J 42(5): 1437-1448. https://doi.org/10.1139/t05-064

Meng X, Wang Y (2016) Modelling and numerical simulation of two-phase debris flows. Acta Geotech 11(5): 1027-1045. https://doi.org/10.1007/s11440-015-0418-4

Ni J, Wu T, Zhu X, et al. (2021) Risk assessment of potential thaw settlement hazard in the permafrost regions of Qinghai-Tibet Plateau. Sci Total Environ 776: 145855. https://doi.org/10.1016/j.scitotenv.2021.145855

Ouyang C, He S, Tang C (2015) Numerical analysis of dynamics of debris flow over erodible beds in Wenchuan earthquake-induced area. Eng Geol 194: 62-72. https://doi.org/10.1016/j.enggeo.2014.07.012

Patle GT, Sikar TT, Rawat KS, et al. (2019) Estimation of infiltration rate from soil properties using regression model for cultivated land. Geol Ecol Landsc 3(1): 1-13. https://doi.org/10.1080/24749508.2018.1481633

Peng J, Fan Z, Wu D, et al. (2015) Heavy rainfall triggered loess–mudstone landslide and subsequent debris flow in Tianshui, China. Eng Geol 186: 79-90. https://doi.org/10.1016/j.enggeo.2014.08.015

Pitman EB, Le L (2005) A two-fluid model for avalanche and debris flows. Philos Trans R Soc A-Math Phys Eng Sci 363(1832): 1573-1601. https://doi.org/10.1098/rsta.2005.1596

Pudasaini SP (2012) A general two - phase debris flow model. J Geophys Res: Earth Surf 117(F3). https://doi.org/10.1029/2011JF002186

Pudasaini SP, Fischer JT (2020) A mechanical erosion model for two-phase mass flows. Int J Multiph Flow 132: 103416. https://doi.org/10.1016/j.ijmultiphaseflow.2020.103416

Puigdefábregas J (2005) The role of vegetation patterns in structuring runoff and sediment fluxes in drylands. Earth Surf Process Landf 30(2): 133-147. https://doi.org/10.1002/esp.1181

Rengers FK, McGuire LA, Coe JA, et al. (2016) The influence of vegetation on debris-flow initiation during extreme rainfall in the northern Colorado Front Range. Geology 44(10): 823-826. https://doi.org/10.1130/G38096.1

Rutgers IR (1962) Relative viscosity of suspensions of rigid spheres in Newtonian liquids. Rheol Acta 2(3): 202-210. https://doi.org/10.1007/BF01983952

Savage SB, Hutter K (1989) The motion of a finite mass of granular material down a rough incline. J Fluid Mech 199: 177-215. https://doi.org/10.1017/S0022112089000340

Stancanelli LM, Peres DJ, Cancelliere A, et al. (2017) A combined triggering-propagation modeling approach for the assessment of rainfall induced debris flow susceptibility. J Hydrol 550: 130-143. https://doi.org/10.1016/j.jhydrol.2017.04.038

Tang C, Zhu J, Li WL, et al. (2009) Rainfall-triggered debris flows following the Wenchuan earthquake. Bull Eng Geol Environ 68(2): 187-194. https://doi.org/10.1007/s10064-009-0201-6

Tang C, Tanyas H, van Westen CJ, et al. (2019) Analysing post-earthquake mass movement volume dynamics with multi-source DEMs. Eng Geol 248: 89-101. https://doi.org/10.1016/j.enggeo.2018.11.010

Zhang Z, Wu Q (2012) Thermal hazards zonation and permafrost change over the Qinghai–Tibet Plateau. Nat Hazards 61(2): 403-423. https://doi.org/10.1007/s11069-011-9923-4

Zhou SY, Gao L, Zhang LM (2019) Predicting debris-flow clusters under extreme rainstorms: a case study on Hong Kong Island. Bull Eng Geol Environ 78(8): 5775-5794. https://doi.org/10.1007/s10064-019-01504-3